Holographic optics for a matched-filter optical processor

J. R. Fienup and C. D. Leonard

The requirements on and the performance of holographic Fourier transform lenses for a matched-filter optical processor are discussed. The holographic aberrations were analyzed using a ray-tracing computer program, and holographic lenses were fabricated and assembled into an optical processor. Analysis and experimental results show that holographic optics are capable of processing images of large space–bandwidth product and can be an attractive alternative to conventional optics.

I. Introduction

Coherent optical processors have proven useful for a number of applications.[1] The unique properties of holographic optical elements offer a number of advantages over glass lenses for use in optical processors. Compared with conventional optics, holographic lenses are thin and light weight. Made by a photographic process, they are potentially inexpensive. They can be made in reflection as well as transmission, allowing for compact folded light paths. Additional advantages include the possibility of multiple functions in the same area of a given hologram (such as focusing, beam splitting, and spectral filtering), multiple superimposed holograms, the ability of a hologram on a curved surface to function independently of shape of the surface, and the ease of recording holographic elements with nonspherical wavefronts.

Reflection holograms recorded in dichromated gelatin can satisfy the requirements of an optical processor for high diffraction efficiency, high angular bandwidth, and low optical noise.[2] Dichromated gelatin holograms of good optical quality can diffract over 95% of the incident light into the first diffracted order and can have angular bandwidths of several degrees.

We analyzed the aberrations of holographic optics in a matched filter optical processor and fabricated and tested an optical processor using holographic lenses. We found holographic lenses to perform well and conclude that they are an attractive alternative to conventional lenses for those applications that can benefit from their unique properties.

The authors are with Environmental Research Institute of Michigan, P.O. Box 8618, Ann Arbor, Michigan 48107.

Received 29 May 1978.
0003-6935/79/050631-10$00.50/0.

II. Analysis of Optics for a Matched-Filter Processor

For comparison, a conventional matched filter optical processor and its holographic optics counterpart are shown in Figs. 1(a) and 1(b), respectively. As previously noted, the striking properties of the holographic optical processor are its compact folded geometry and its light weight. Referring to Fig. 1, the input (signal) transparency S, which has amplitude transmittance $s_1(x)$, is illuminated by a plane wave from the collimator H_c (or L_c). We use 1-D notation for simplicity; the extension to two dimensions is obvious. In the ideal case, the first Fourier transforming element H_1 (or L_1) causes the wavefront $S_1(u) = \mathcal{F}[s_1(x)]$, the Fourier transform of $s_1(x)$, to appear at the filter plane. The matched filter has been made to have an effective transmittance $S_2^*(u) = \{\mathcal{F}[s_2(x)]\}^*$, where $s_2(x)$ is a reference image, and * denotes the complex conjugate. The second Fourier transforming element (also referred to as the reimaging element) H_2 (or L_2) causes the Fourier transform of $S_1(u)S_2^*(u)$, the wavefront emerging from the filter, to appear at the output plane OD. For simplicity, assume that the focal lengths of the two Fourier transforming elements are the same. The amplitude of the output is given by

$$g(x) = s_1(x) \star s_2(x) = \int_{-\infty}^{\infty} s_1(x_1)s_2^*(x + x_1)dx_1, \qquad (1)$$

which is the desired cross-correlation. In Eq. (1), constant factors that depend on optical parameters are ignored. If the input image is simply the reference image shifted so that it is centered at x_0, the output becomes the autocorrelation

$$g(x) = \int_{-\infty}^{\infty} s(x_1)s^*(x + x_0 + x_1)dx_1, \qquad (2)$$

which has its peak at $-x_0$:

$$A_0 = g(-x_0) = \int_{-\infty}^{\infty} |s(x_1)|^2 dx_1 = \int_{-\infty}^{\infty} |S(u)|^2 du, \qquad (3)$$

where the second line of the equation above results from Parseval's theorem.

As with conventional optics, holographic optics have aberrations that limit the performance of optical processors. For conventional optics, aberrations can be reduced by the use of well designed multiple-element lens systems. However, a similar reduction of aberrations is usually not practical with holographic optics. Holographic elements ordinarily must be separated by a considerable distance in order to separate the desired order of diffraction from the spurious ones, although this effect is minimized by volume phase holograms. For reflection holograms, the element following the hologram cannot be allowed to block the beam incident on the hologram. Furthermore, due to their off-axis nature, a group of hologram lenses would be more difficult to align than on-axis optics. Besides, the use of multiple-element holographic optics would negate the advantages of light weight and low cost. For these reasons, we restricted our attention to simple single-element holographic lenses on plane substrates.

Unlike a simple lens with spherical surfaces, a holographic lens recorded with spherical wavefronts will introduce no phase errors if illuminated with the wavefront for which it was made. However, as the curvature and field angle of the incident wavefront differ from the reference beam used to record the hologram, aberrations appear, as analyzed by Champagne.[3] The chromatic aberrations are not a factor since the optical processor can operate with monochromatic light of the same wavelength used to record the hologram. Since a hologram lens in an optical processor operates on a complex wavefront comprised of the sum of many wavefronts of various field angles, it necessarily exhibits aberrations.[4] The nonchromatic holographic aberrations are the limiting factor in the performance of the processor.

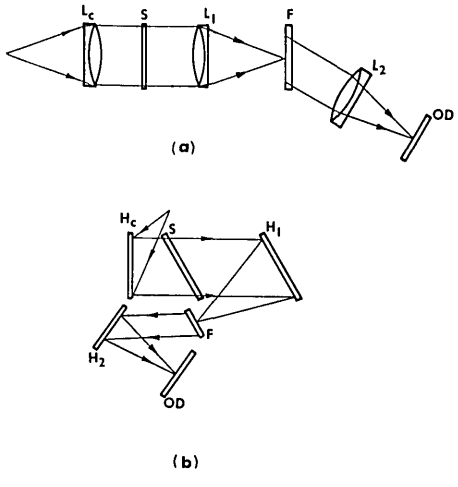

Fig. 1. Configurations of optical processors using (a) conventional optics and (b) holographic optics.

A. Standard Deviation Criterion

In order to specify the maximum tolerable aberrations that the Fourier transforming elements can be allowed to introduce, it is first necessary to determine, in general, the effects of aberrations in the Fourier transforming elements on the correlation output of the matched filter optical processor. However, due to the operation of the matched filter combined with the space variance of the aberrations, it is not possible to analyze the entire system by conventional wavefront analysis or ray-tracing methods. Therefore, it is necessary to simplify the analysis, say, by treating only one element at a time. In order to judge a single Fourier transforming element, we used a standard deviation error criterion, which is derived below. This derivation applies to conventional as well as holographic optics.

Referring again to Fig. 1, suppose that H_1 introduces a phase error $\phi_1(x)$. Strictly speaking, ϕ_1 is a function not only of the hologram coordinate, but also of the coordinate u of the filter plane, that is, ϕ_1 is space variant. We will continue this derivation with the simplification that ϕ_1 is space invariant; a justification for this simplification will be given later. A further simplification is that the phase error ϕ_1 is introduced near the input plane. This is strictly true for certain processor geometries and approximately true for slowly varying phase errors for the geometry of Fig. 1. The justification of the latter simplification relies on the fact that slowly varying phase wavefronts change slowly as they propagate. Since the phase errors involved are, in fact, small and slowly varying, this is a good approximation. Thus, for a slowly varying phase error ϕ_1, the wavefront arriving at the filter is proportional to

$$\left[S(u)\exp\left(-j\frac{2\pi}{\lambda f}ux_0\right)\right] * \mathcal{F}[\exp(j\phi_1)], \tag{4}$$

where λ is the wavelength of light, f is the focal length of the Fourier transforming element, x_0 is the translation of the center of the input from the optical axis, and $*$ denotes convolution. This wavefront, multiplied by the filter function $S^*(u)$, is approximately an apodized plane wave. (If no phase errors were present, its phase would be $-2\pi ux_0/\lambda f$.) It is Fourier transformed and brought to focus in the output plane by H_2, which introduces a slowly varying phase error ϕ_2 (which depends on x_0). The amplitude of the wavefront at the output is given by

$$g(x) = \mathcal{F}\left(\left\{\left[S(u)\exp\left(-j\frac{2\pi}{\lambda f}ux_0\right)\right] * \mathcal{F}[\exp(j\phi_1)]\right\}S^*(u)\exp(j\phi_2)\right). \tag{5}$$

For the geometry of Fig. 1, the matched filter introduces only distortion,[5] which is ignored here since it has no effect on the detectability of the output peak and can ultimately be corrected by postdetection compensation. If no phase errors are present, $\phi_1 = \phi_2 = 0$, then Eq. (5) reduces to Eq. (2).

The effects of phase errors ϕ_2 are made more clear by setting $\phi_1 = 0$ in Eq. (5), which then reduces to

$$g(x) = \int_{-\infty}^{\infty} |S(u)|^2 \exp[j\phi_2(u)]\exp\left[-j\frac{2\pi}{\lambda f}u(x+x_0)\right]du. \tag{6}$$

Evaluating at the central peak, $x = -x_0$, the ratio of the intensity of the central peak to its theoretical maximum value is

$$R = \frac{|g(-x_0)|^2}{A_0^2} = \frac{\left|\int_{-\infty}^{\infty} |S(u)|^2 \exp[j\phi_2(u)]du\right|^2}{\left|\int_{-\infty}^{\infty} |S(u)|^2\, du\right|^2}$$

$$= \left|\sum_{k=0}^{\infty} \frac{(j)^k}{k!} \cdot \frac{\int_{-\infty}^{\infty} |S(u)|^2 \phi_2^k(u)du}{\int_{-\infty}^{\infty} |S(u)|^2 du}\right|^2$$

$$\equiv \left|\sum_{k=0}^{\infty} \frac{(j)^k}{k!} \overline{\phi_2^k}\right|^2, \tag{7}$$

where $\overline{\phi_2^k}$ is a weighted average of the kth power of $\phi_2(u)$. The weighting function $|S(u)|^2$ is simply the intensity pattern of the wavefront emerging from the spatial filter. For reasons described later, this weighting function can be approximated by a constant over the width of the filter. For small phase errors, assuming $\overline{\phi^k} \ll 1$ for $k \geq 3$, Eq. (7) becomes

$$R \simeq 1 - \overline{\phi_2^2} + \overline{\phi_2}^2 = 1 - \sigma_2^2, \tag{8}$$

where

$$\sigma_2 = (\overline{\phi_2^2} - \overline{\phi_2}^2)^{1/2} \tag{9}$$

is the standard deviation of the phase error. That is, for small phase errors, the autocorrelation peak intensity is independent of the type of phase error present and depends only on σ_2. This relationship between the normalized intensity and the standard deviation (sometimes loosely referred to as the rms) of the phase error is the familiar formula for the Strehl intensity. This is expected since the function of H_2 is essentially to bring to focus a pointlike image. Linear phase errors introduced by H_2 shift the peak in the output plane (distortion) without degrading the peak itself. Since slight position errors may be acceptable or calibrated out of the system, linear phase errors should not be included in the calculation of σ_2.

The effects of phase error ϕ_1, introduced by the first Fourier transforming element H_1, are made more clear by setting $\phi_2 = 0$ in Eq. (5), which then reduces to

$$g(x) = \int_{-\infty}^{\infty} s(\xi) \exp[j\phi_1(\xi + x_0)] s^*(\xi + x_0 + x)d\xi. \tag{10}$$

Evaluating at the peak, $x = -x_0$, this becomes

$$g(-x_0) = \int_{-\infty}^{\infty} |s(\xi)|^2 \exp[j\phi(\xi + x_0)]d\xi. \tag{11}$$

Again expanding the exponential and interpreting the integral as a weighted sum of the phase errors, we find that for small phase errors

$$R \simeq 1 - \sigma_1^2, \tag{12}$$

where $\sigma_1 = (\overline{\phi_1^2} - \overline{\phi_1}^2)^{1/2}$ is the standard deviation of the phase error introduced by H_1. Unlike σ_2, σ_1 includes the contributions from linear terms. Thus, the normalized peak intensity of the autocorrelation output of a matched filter optical processor decreases with the square of the standard deviation of the phase error not only for the second reimaging Fourier transforming element, but also for the first Fourier transforming element. This relationship allows the use of a very simple quality criterion for evaluating the Fourier transforming elements for a matched filter optical processor.

The approximations assumed in the derivation of Eq. (5) were that σ_1 be small, slowly varying, and space-invariant. While σ_1 generally will be small and slowly varying, it will not be space-invariant. In most cases, σ_1 increases with increasing field angles or, equivalently, with increasing $|u|$ in the filter plane and is maximum for u coordinates at the edge of the filter plane. The justification for the space-invariance approximation is as follows. Since the purpose of the matched filter optical processor is to produce a sharp peak in the output plane, it is the value of σ_1 for points near the edge of the filter plane that determines the performance of the processor. Using σ_1 at the edge of the filter is appropriate, since the information at the edges of the matched filter is ordinarily emphasized in order to increase the selectivity of the filter and increase the sharpness of the autocorrelation peak.[6] This is usually unavoidable since it is difficult to record the large dynamic range of $S^*(u)$ in the matched filter; but it is also highly desirable. The wavefront emerging from the matched filter has an intensity distribution that is more nearly constant or of an annular shape, rather than being sharply peaked in the center as $|S(u)|^2$ would be. In this case, the output is no longer truly an autocorrelation; it more closely resembles a point image. Thus, we are led to base our analysis of the performance of element H_1 on the value of σ_1 for field angles corresponding to the edges of the filter.

A further justification of basing the analysis on σ_1 at the edge of the filter is as follows. Suppose that for a given input size and system design, σ_1 goes beyond a certain critical level (the value of that critical level will be shown later) for positions in the filter plane with $|u| > |u_{\max}|$. Then an aperture should be placed at the filter plane to block out the portion of the wavefront for which $|u| > |u_{\max}|$, since that portion of the wavefront will lead to a degradation rather than a reinforcement of the autocorrelation peak at the processor output. That value of $|u_{\max}|$ defines the size of the filter used and, consequently, the maximum spatial frequency component of the input transparency that is used. Thus, the maximum usable space–bandwidth product of the input and the resolution at the output is determined by the value of $|u_{\max}|$ for which σ_1 goes above the critical level. One can therefore ignore the space variance of the phase error ϕ_1 and concentrate on the value of σ_1 as computed for the edge of the matched filter.

To test the validity of Eq. (12) and to establish more accurately the effects of phase errors ϕ_1, we digitally computed the aberrated autocorrelation integral of Eq. (5) with $\phi_2 = 0$ for the hypothetical 1-D object shown in Fig. 2(a) with various phase errors ϕ_1. Figure 2(b) shows the central portion of the autocorrelation output with no phase error (uppermost curve) and with $\sigma_1 = 1/16$ wavelength nth-order phase error for $n = 1$–4, respectively. That is, one curve results from a linear phase error of 0.2165 wavelengths peak-to-peak, the second

from a quadratic phase error of 0.2097 wavelengths, etc. The peaks of all four curves fall into the range of 0.842–0.868, in very good agreement with the value $1 - (2\pi/16)^2 = 0.846$ predicted by Eq. (12). Figure 2(c) shows the same thing with $\sigma_1 = 1/8$ wavelength. In this case, the peaks fall in the 0.478–0.567 range, not in very good agreement with the 0.383 value predicted by Eq. (12). Figure 2(d) shows the same thing with $\sigma_1 = 1/4$ wavelength. From Figs. 2(c) and 2(d), it is apparent that Eq. (12) is no longer reliable for $\sigma_1 \geq 1/8$ wavelength. However, for σ_1 much greater than 1/8 wavelength, the autocorrelation peak would no longer be detectable.

From the above results, we can formulate the following standard deviation phase error criterion: the standard deviation of the total phase error should be kept to 1/8 wavelength in order to insure that the autocorrelation peak remain easily detectable. This corresponds to the following peak-to-peak errors (in wavelengths): 0.433 of linear; 0.419 of quadratic; 0.660 of cubic; and 0.468 of fourth-order. As shown in Fig. 2(c), $\sigma_1 = 1/8$ wavelengths results in a greatly reduced, but still detectable, autocorrelation peak; and as shown in Fig. 2(d), $\sigma_1 = 1/4$ wavelengths results in an autocorrelation peak that would be lost in the noise.

As discussed earlier, it is desirable to record the matched filter in a nonlinear way so as to block the lower and emphasize the higher spatial frequencies. In a computer simulation, this effect was approximated in Eq. (5) by multiplying $S^*(u)$ by a high-pass stop of the form $[1 - \text{rect}(u/u_a)]$. As expected, this resulted in an output peak that is much sharper and has a higher SNR. An example of this is shown in Fig. 2(e), for which $\sigma_1 = 0$, and the high-pass stop was 20% of the total filter-plane aperture width. Figure 2(f) shows the results with $\sigma_1 = 1/4$ wavelength nth order phase error for $n = 1$–4, respectively. Since the output peaks are easily detectable above the noise, these curves suggest that the emphasis of the higher spatial frequencies also serves to make the process less sensitive to the slowly varying phase errors. Thus, the standard deviation phase error quality criterion developed above for the case of linear filter recording should be taken as a lower bound on the performance of the Fourier transforming lens.

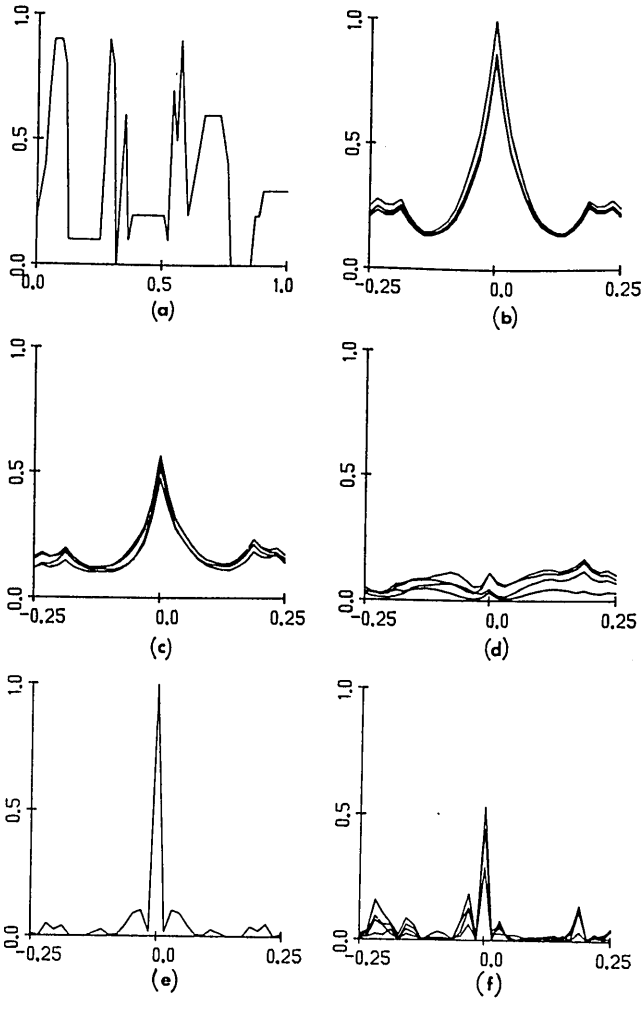

Fig. 2. Computer simulation of matched filter output with aberrations: (a) test object; (b)–(f) central portions of aberrated autocorrelation outputs: (b) no phase error (uppermost curve) and $\sigma_1 = \lambda/16$ nth order phase error, $n = 1$–4; (c) $\sigma_1 = \lambda/8$; (d) $\sigma_1 = \lambda/4$; (e) 20% central stop, no phase error; (f) 20% central stop, $\sigma_1 = \lambda/4$.

B. Aberration Computation

Champagne's equations[3] can be used to compute the third-order holographic aberrations, but they are inconvenient for computing the standard deviation phase error σ. Furthermore, they do not include higher-order aberrations without adding considerable complexity. Consequently, to analyze and optimize accurately and efficiently the design of the holographic optics, we used a holographic ray-tracing computer program called the Holographic Optics Analysis and Design (HOAD) program, developed at ERIM.[7]

The hologram H_c shown in Fig. 1(b) is a collimator and is reconstructed in exactly the same way that it was recorded. Consequently, it has no holographic aberrations and produces an ideal plane wave.

In analyzing H_1, the first Fourier transforming element, it is important to note that, whatever aberrations H_1, introduces, if the same element is used to record the matched filter, it is a matched filter of an aberrated reference image. If the untranslated reference image is used as the input, and the same aberrations are introduced, it should correlate perfectly. This would seem to indicate that a very poor lens could be used for H_1, and, indeed, that is the case if the image is not translated in the input. However, as the input is translated, the effective aberrations change, and the correlation peak degenerates. Thus, the phase error of interest is not the absolute phase error, but is the difference between the phase error when the center of the input image is translated to x_0 and the phase error when the center of the image is on the optical axis (i.e., as the matched filter was recorded). Consequently, some of the requirements for the Fourier transforming lens, for example, that the Abbe sine condition must be fulfilled,[8] may be relaxed. Generally, the phase error differences

are minimized when the absolute phase error is minimized, and low-aberration lenses are required for the matched filter optical processor.

To analyze H_1, we considered one plane-wave spatial frequency component of the input at a time, by tracing crossed fans of parallel rays at a given field angle from the input plane, through H_1, to the filter plane. Often the translation x_0 of the input image relative to the reference image is comparable in size to, or larger than, either the input image or the reference image. (In many applications, one of the two images covers a much smaller area than the other—we refer to the smaller of the two as the image of interest.) In that case, the predominant term in the difference of the phase errors is linear. That is, the predominant effect is that if a plane-wave component of the image comes to focus at u_1 when the image is centered on the optical axis, then it will come to focus at $u_1 + \Delta u$ when the image is centered at x_0; and the linear phase term is proportional to Δu. The difference of the phase errors can be approximated by computing the aberrations of the plane-wave component of the input image with respect to the position u_1 in the filter plane (rather than computing the aberrations with respect to its own image point at $u_1 + \Delta u$).

The analysis of H_2 is simpler, since it only brings a quasi-plane wave to focus at the output, and linear phase errors are not considered significant. Because of this, the requirements on H_2 are not as stringent as on H_1, nor are they as stringent as they would be for some other types of processors.

C. Optimization and Analysis

Holographic optics has a somewhat different set of parameters for design optimization than is available to conventional optics. The over-all geometry of a holographic optical system can be adjusted by appropriate choices of focal lengths, offset angles, and transmissive vs reflective holograms. Since the gross imaging properties of an individual holographic element do not depend on the angular orientation or shape of its surface, the angular orientation of the element with respect to the rest of the system and the curvature of the surface of the hologram substrate can be designed to minimize aberrations. A hologram can be made at one wavelength and read out at a second wavelength. The thickness and refractive index modulation of a holographic element can be manipulated to produce a desired Bragg angular and wavelength selectivity. Analogous to conventional lenses, holographic elements of a given focal length can have different shape factors, depending on the curvatures of the reference and object beams used to record the hologram.

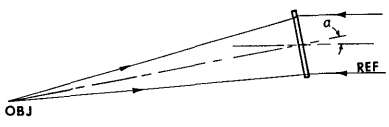

Fig. 3. Recording geometry for 10° offset Fourier transforming holographic lens.

In general, aberrations tend to be minimized when the offset angles are minimized, so the minimum offsets allowed by the system geometry were used. It was assumed that the processor operates at the same wavelength, 514.5 nm, at which the holograms are recorded, which also tends to minimize aberrations. In order to keep the system as simple and economical as possible, only single elements on plane surfaces were considered.

1. *Before-the-Lens Processor*

Using the HOAD program, we optimized the shape factors of H_1 and H_2 and their angular orientations with respect to the rest of the system. As depicted in Fig. 1(b), H_1 and the filter should be parallel to one another and normal to the axis between them. Similarly, H_2 and the output plane should be parallel to one another and normal to the axis between them. (Note that the input plane S is parallel to H_1, as shown, making it tilted with respect to the S–H_1 axis. If S is rotated to be normal to the S–H_1 axis, the output plane OD rotates to become parallel to S, but tilted with respect to the H_2–OD axis.) The recording geometry for H_1 is shown in Fig. 3 for a 10° offset, where the point source for the object beam is located at the center of the filter plane, and the reference beam is a plane wave conjugate to the S–H_1 axis. The recording geometry of H_2 is the mirror image of Fig. 3, where the point source for the object beam is located at the center of the output plane, and the reference beam is a plane wave conjugate to the filter–H_2 axis.

The HOAD program was used to compute σ_1, the standard deviation phase error of H_1, as a function of field angle (or filter plane location), diameter D_s of the image of interest, translation x_0 of the input, and focal length. The performance can be determined, for example, by fixing all the parameters except x_0, then increasing x_0 until σ_1 equals $\frac{1}{8}$ wavelength. This, along with the diameter of the image of interest, defines $D = D_s + 2x_0$, the greatest width of an image that can be processed, that is, within which the image of interest can be located and still produce a detectable correlation peak. Combined with the field angle (corresponding to the maximum spatial frequency component of the image), the width gives the maximum space–bandwidth product (number of picture elements) that can be processed without a loss of resolution.

Two families of operating curves for a 100-mm focal-length H_1 are shown in Fig. 4. The varying parameters for the different curves are D_s and the maximum spatial frequency, respectively. These curves may be used as follows. If it is required that the resolution of the matched filtering operation be equivalent to 20 cycles/mm in the input plane and that the image of interest be detectable anywhere within a total image area of 750 × 750 picture elements, the image of interest could contain no more than 100 × 100 picture elements. Two facts made evident by Fig. 4 are that the performance improves if the image is demagnified (i.e., it performs better for higher spatial frequencies, but

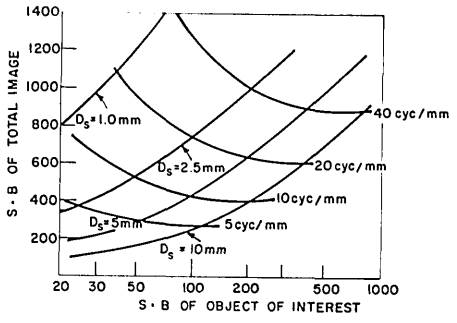

Fig. 4. Performance of a 100-mm focal length Fourier transforming holographic lens: the linear space–bandwidth product of the total image vs the linear space–bandwidth product of the area of interest, for various values of the width D_s of the area of interest and of the maximum spatial frequency of the image.

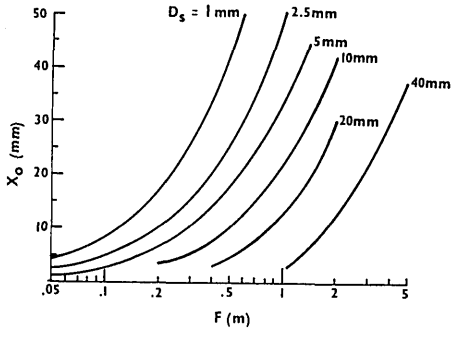

Fig. 5. Translation x_0 of the input resulting in $\sigma_1 = \lambda/8$, vs focal length F, for various widths D_s of the image of interest. A 10° offset and 40-cycle/mm spatial frequency are assumed, making 10 mm equivalent to 800 picture elements.

proportionally smaller image widths) and that there is a trade-off between D_s and D (i.e., the larger the image of interest, the less it can be translated).

The aberrations of the second Fourier transforming element H_2 were also computed. Since it was found that the aberrations of H_1 generally were the limiting factor in the performance of the system, the less interesting results on H_2 will not be given here.

A most important parameter is the focal length F of the Fourier transforming elements. Using Champagne's equations,[3] it can be shown that, for a given image size and field angle, third-order coma is proportional to $1/F^2$, and third-order astigmatism is proportional to $1/F$. Consequently, the performance of the processor improves greatly with increasing focal lengths. As an example, Fig. 5 shows the translation x_0 that results in $\sigma_1 = \frac{1}{8}$ wavelength vs focal length for various values of D_s. A highest spatial frequency of 40 cycles/mm and an offset of 10° were assumed. In this case, 10 mm is equivalent to 800 picture elements. Figure 5 indicates that a compact processor using elements with short (100-mm) focal lengths can process imagery of a few hundred picture elements on a side; and if long (>1-m) focal lengths are allowed, the holographic optics can handle imagery having thousands of picture elements on a side.

2. *After-the-Lens Processor*

An alternative to the configurations shown in Fig. 1 is to locate the input plane in a converging beam after a transmissive first Fourier transforming lens,[9] which would allow for easy changes in scale by translating the input along the optical axis. In this case, the first Fourier transforming element, which could be combined with the collimator, would produce a perfect converging spherical wavefront. Nevertheless, the resulting Fourier transform would be aberrated everywhere except on axis (in addition to having a spherical phase factor associated with the Fourier transform). The Fourier transforming property of a converging beam is valid only under the paraxial approximation.

In order to analyze the aberrations of the after-the-lens Fourier transform geometry, consider a single spatial frequency component of the input. For a given spatial frequency component, the input can be modeled as a constant-frequency holographic grating with recording parameters $R_R = R_O = +\infty$, $\alpha_R = \beta_R = 0$, and α_O and β_O are the angles corresponding to the spatial frequency under consideration. For this analysis, we use Champagne's notation and equations,[3] in which R is the radial distance of a recording or reconstruction point source from the hologram, α and β are field angles, and subscripts R, O, C, and I refer to reference, object, reconstruction, and image beams, respectively. For simplicity, consider $\beta_O = 0$, since the performance will be symmetric in the x and y dimensions. The reconstruction beam is the spherical wave converging to the center of the matched filter plane and is given by $R_C = -F$ and $\alpha_C = \beta_C = 0$. Then Champagne's equations for the image location reduce to

$$R_I = R_C = -F, \tag{13}$$

$$\sin\alpha_I = \sin\alpha_0, \text{ or, } \alpha_I = \alpha_0 \equiv \alpha, \tag{14}$$

$$\cos\alpha_I \sin\beta_I = \cos\alpha_C \sin\beta_C = 0; \tag{15}$$

and the coefficients of the third-order aberrations reduce to

$$S = \frac{1}{R_C^3} - \frac{1}{R_I^3} = 0, \tag{16}$$

$$C_x = -\frac{\sin\alpha_I}{R_I^2} = -\frac{\sin\alpha}{F^2}, \tag{17}$$

$$C_y = 0, \tag{18}$$

$$A_x = -\frac{\sin^2\alpha_I}{R_I} = \frac{\sin^2\alpha}{F}, \tag{19}$$

$$A_y = A_{xy} = 0, \tag{20}$$

where the coefficients S, C, and A are for aberrations of the spherical, comatic, and astigmatic types, respectively.

It is interesting to compare these aberrations with those of the before-the-lens processor. For the before-the-lens processor, using the holographic element shown in Fig. 3, the recording parameters are $R_R = -\infty$, $R_O = F$, $\alpha_R = 10°$, and $\beta_R = \alpha_O = \beta_O = 0$; and for the

reconstruction, $R_C = \infty$, and α_C and β_C are variable. If β_C is set to zero and $\sin\alpha$ is substituted for $\sin\alpha_C - \sin\alpha_R$, it can be shown that the aberration coefficients of the optimized holographic before-the-lens processor are the same as those given above the after-the-lens processor. The aberrations in the two cases are not exactly the same, however, since a given plane wave spatial frequency component of the input to the before-the-lens processor arrives at H_1 off center by a distance $F \sin\alpha$. Nevertheless, using the HOAD program it was found that, for the range of parameters studied, the performance of the after-the-lens processor differs very little from that of the holographic before-the-lens processor.

In addition to allowing scale changes, the after-the-lens processor allows for a distance of F between the input and filter planes, as compared with $2F$ for the before-the-lens processor. (This advantage is diluted, however, since the before-the-lens processor can be folded to reduce the $2F$ length back to F.) Furthermore, for longer focal length systems for which αF is comparable with D, the Fourier transforming element in the after-the-lens processor can be smaller than that of the before-the-lens processor. A disadvantage of the after-the-lens processor is that since the matched filter is required to record an additional spherical phase factor, the matched filter itself will introduce aberrations not present in the matched filter made for a before-the-lens processor.[5,9]

3. *Fourier Spectrum Analysis*

The holographic Fourier transforming lenses were also analyzed for use in simple Fourier transform optical processors for performing Fourier spectrum analysis of an input transparency. Such a processor would be similar to the first half of the matched-filter optical processor, with the output plane being located in place of the matched filter. For this analysis, the distortion of the output (linear phase errors) was ignored, and it was assumed that the optimized holographic lens shown in Figs. 3 with a 10° offset angle is used, and it was required that σ not exceed $\frac{1}{8}$ wavelength at 40 cycles/mm in the input. Figure 6 shows the predicted linear space–bandwidth product of the input that could be Fourier transformed (which is proportional to the maximum allowed width of the input) as a function of the focal length of the holographic lens.

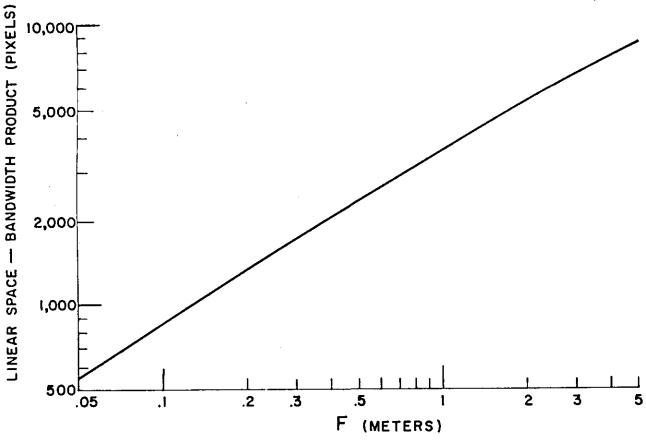

Fig. 6. Performance of holographic lens for Fourier spectrum analysis, assuming $\sigma \leq \lambda/8$ at 40 cycles/mm.

III. Hologram Fabrication

Dichromated gelatin plates were prepared by fixing the silver halide out of 5 × 5-in. (12.7 × 12.7-cm) Kodak 649-0 microflat plates, then sensitizing with ammonium-dichromate solution. The processing procedures used were those of Chang and Leonard,[2] which are similar to those of Chang.[10] Because of the physical sizes of the plate holders and other available equipment, we chose the focal lengths and offset angles of the two Fourier transforming lenses to be 500 mm and 20°, respectively. Using the 514.5-nm wavelength from an argon-ion laser, typical exposures were at 1 mW/cm^2 for 8 min.

The emulsion side of the plate was placed away from the point source during recording and away from the input and filter planes when in the processor. Consequently, the input wavefront passes through the glass substrate both before and after reflection from the holographic lens. The spherical aberration introduced by the glass substrate into the diverging recording beam is canceled by the opposite aberration introduced by the substrate into the converging reflected wavefront upon readout. An advantage of this orientation of the emulsion is that the reconstructed beam is reflected without passing through the outer surface of the emulsion. Then the dichromated gelatin hologram can be sealed (to protect the emulsion primarily from the effects of humidity) by cementing on a thin glass cover plate, without having to consider the optical quality of the cover plate.

The diffraction efficiency of a typical holographic lens made for the experiments is 70%. Heavier exposures resulting in higher diffraction efficiencies were avoided since they also result in the recording of spurious holograms. The spurious holograms arise from beams internally reflected from the air–glass and air–gelatin surfaces. For the highest quality results, those unwanted reflections can be eliminated by recording the hologram in a liquid gate with antireflection windows.

The diffraction efficiency of the holographic lenses must remain high for a range of angles of illumination. For the first Fourier transforming lens, the required angular bandwidth is $\pm\alpha_m$, where α_m is the angle corresponding to the maximum spatial frequency of the input; for example, $\alpha_m = 1.18°$ for a frequency of 40 cycles/mm. For the second Fourier transforming lens, the required angular bandwidth is $\pm\arctan(x_m/F)$, where x_m is the largest allowed translation of the input; for example, if $x_m/F = 25$ mm/500 mm, the required angular bandwidth is ±2.86°. The angular bandwidths of the holographic lenses were made to satisfy easily these requirements, as can be seen from the curves

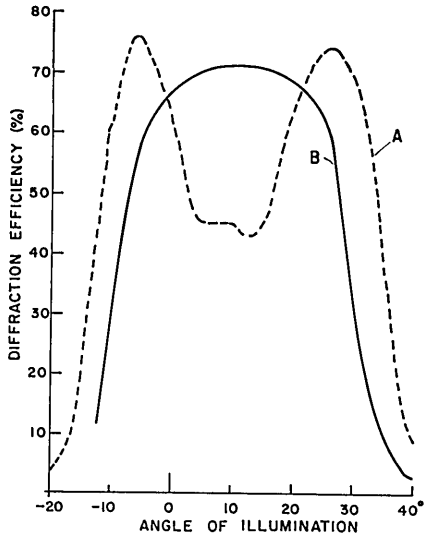

Fig. 7. Diffraction efficiency vs angle of illumination for holographic lenses A and B.

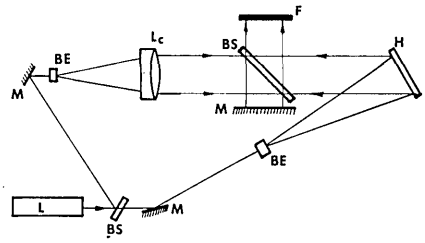

Fig. 8. Interferometer for testing holographic lenses.

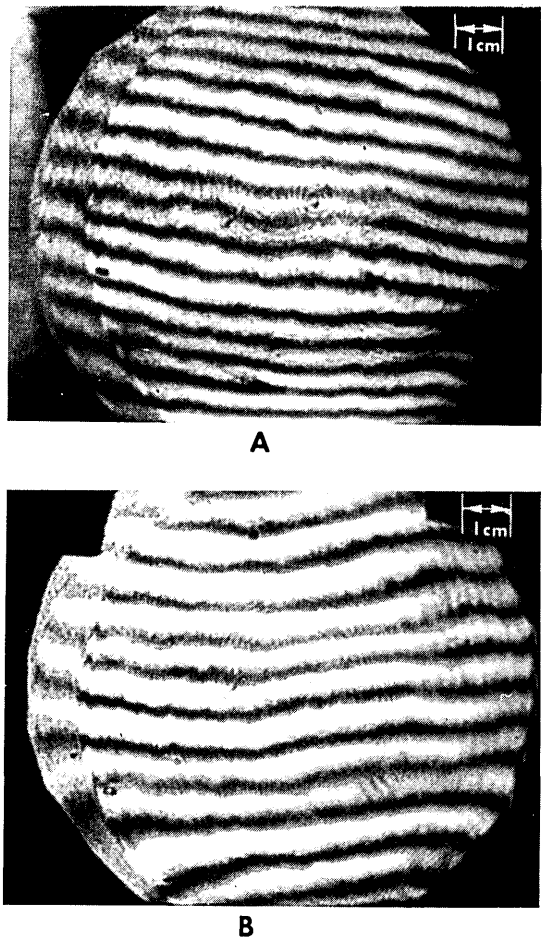

Fig. 9. Interferograms of holographic lenses A and B.

shown in Fig. 7 of diffraction efficiency vs angle of illumination for the central portions of two different holographic lenses. Both holographic lenses were recorded with 20° offset angles and are designed to operate at angles about 20°. The double peaks in curve A arise from the symmetry of the Bragg condition about the angle of approximately 10° to which the fringe planes are normal. The right peak of curve A is at an angle greater than 20° due to an increase in the thickness of the hologram emulsion. A decrease in the emulsion thickness caused the peaks of curve B to move together to form a single broad peak. The emulsion thickness is controlled primarily by the concentration of the sensitizer. The thickness can then be fine-tuned during the drying process in which the holograms are baked in an oven under vacuum, which drives moisture from the emulsion. The emulsion thickness can be decreased by additional baking. If the emulsion is baked excessively and becomes too thin, it can be made thicker by immersing it in water and baking it again to a lesser degree. In this way the peak of the angular selectivity curve can be adjusted as desired, within certain limits.

The high angular bandwidths of the holographic lenses result from large refractive index modulations, determined to be approximately 0.07. Higher modulation could be achieved, but at the expense of optical quality.

Our primary consideration was the phase aberrations of the holographic lenses. Before preparing them for exposure, the best samples from a few boxes of 679-0 plates were selected, based on examination of flatness using a Mach-Zehnder interferometer. Since washing and sensitization of the plates were done after the interferometric test, it did not matter that the plates were exposed to light during the test. After being recorded and processed, the holograms were tested for aberrations using the interferometer geometry shown in Fig. 8. The position of the point source illuminating the hologram was the same as that used to record it, and so there are no theoretical holographic aberrations. The aberrations that appear in this configuration (the nonholographic aberrations) are due, primarily, to variations in emulsion thickness and edge effects. Figure 9 shows interferograms of 10-cm diam of two different holographic lenses used in our experiments. The peak-to-peak phase error of lens A is about $\lambda/4$ over a 4-cm diam and $\lambda/2$ over an 8-cm diam, and of lens B it is about $\lambda/4$ over a 4-cm diam and about $\lambda/2$ over a 6-cm diam. These aberrations are sufficiently low for the purposes of our experiments.

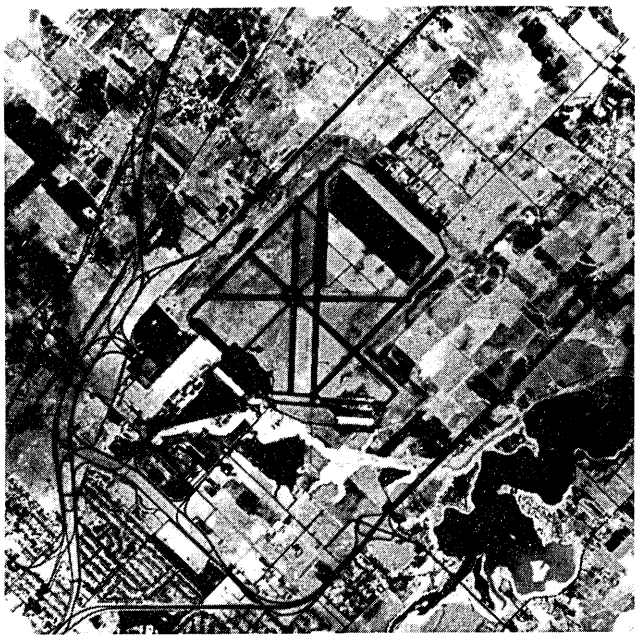

Fig. 10. Input image for correlation experiments.

IV. Correlation Experiments

The holographic lenses described in the previous section were assembled into a matched filter optical processor, and matched filtering experiments were performed. Matched filters on 4 × 5-in. (10 × 12.7-cm) Kodak 131-01 microflat plates were recorded with the image centered in the input plane and using H_1 to perform the Fourier transform; referring to Fig. 1(b), the reference beam was a plane wave along the filter-to-H_2 axis. The intensities of the reference and signal beams were adjusted so that the fringe contrast was highest for spatial frequencies above 15 cycles/mm. This resulted in matched filters that are opaque in their central regions because of heavy overexposure. The filters, giving heavy weighting to the higher spatial frequencies, resulted in very sharply peaked correlation outputs.[6]

In one experiment, the matched filter was recorded of a 25-mm diam area of the input image shown in Fig. 10. The filter was limited to a 13.5-mm diam aperture, corresponding to a field angle of 0.77° and a spatial frequency of 26 cycles/mm. The central 3.5-mm diam area of the filter was opaque, resulting in an active area of the filter having an annular shape. A photometric scan through the correlation peak for $x_0 = 4$ mm is shown in Fig. 11. The half-power width of the peak shown is about 31 μm, and it is more than 30 dB above the noise. The sidelobe ring around the main peak is a characteristic of the annular shape of the matched filter. The intensity of the correlation peak as a function of input translation x_0 is shown in Fig. 12. Even at $x_0 = 21$ mm, for which its intensity is 15% of its value for $x_0 = 0$, the peak, though aberrated, is easily detectable and is 28 dB above the noise, as shown in Fig. 13.

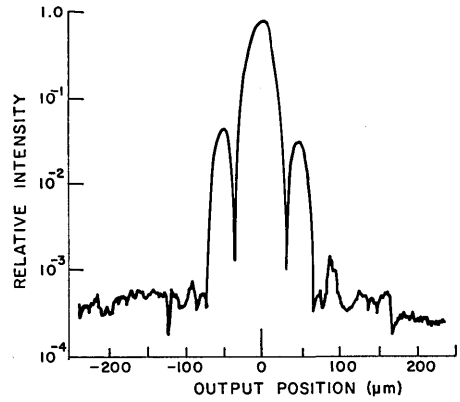

Fig. 11. Scan through peak of output, $x_0 = 4$ mm.

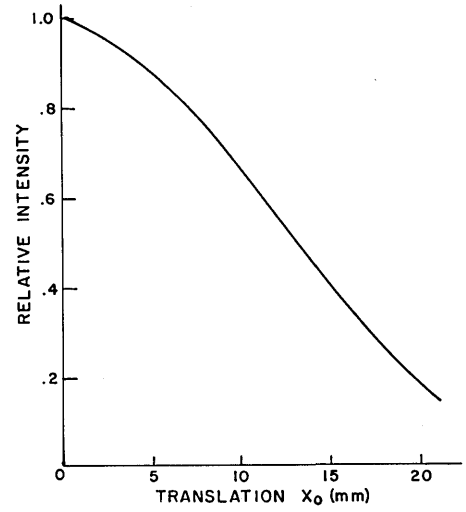

Fig. 12. Intensity of output peak vs x_0.

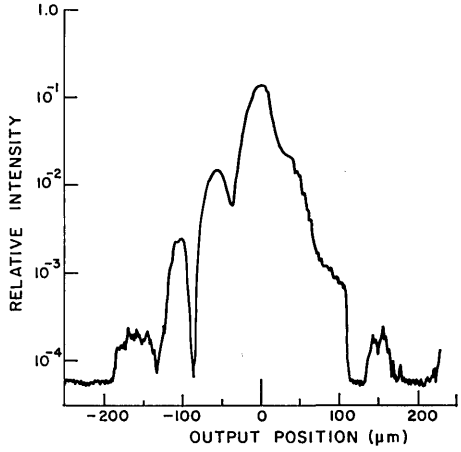

Fig. 13. Scan through peak of output, $x_0 = 21$ mm.

The performance of the holographic optics indicated by the results above is somewhat better than that predicted by the standard deviation phase error criterion. For an input of 25-mm diam and a field angle of 0.77°, the HOAD program predicts $\sigma_1 = 1/8$ wavelength for $x_0 = 10$ mm; but the measured peak intensity does not drop to 50% until $x_0 = 13.5$ mm and is easily detectable for x_0 beyond 21 mm. This discrepancy is due to the inaccuracy of the space invariance assumption and the decreased sensitivity of the processor to slowly varying phase errors when the higher spatial frequency information is emphasized. Thus, the standard deviation phase error criterion should be taken as a lower bound on the performance of the processor.

V. Conclusions

Analysis was performed and experiments verified that holographic optics can perform well as the Fourier transforming elements of a matched-filter optical processor. The aberrations of a holographic before-the-lens processor were found to be comparable with those of an after-the-lens processor. Holographic optics of a simple design are capable of processing imagery of a large space–bandwidth product if long enough focal lengths are allowed. The standard deviation phase error criterion was found to be a useful guide for predicting the performance of the lenses in a matched-filter optical processor.

This work was supported by the Air Force Office of Scientific Research under contract F44620-76-C-0047.

References

1. A. Vander Lugt, Proc. IEEE **62,** 1300 (1974).
2. B. J. Chang and C. D. Leonard, to be submitted to Appl. Opt.
3. E. B. Champagne, J. Opt. Soc. Am. **57,** 51 (1967); E. B. Champagne, "A Qualitative and Quantitative Study of Holographic Imaging," Ph.D. Thesis, Ohio State University, Columbus, July 1967 (University Microfilms 67-10876).
4. This point was not understood by P. C. Mehta, S. Swami, and V. V. Rampal, Appl. Opt. **16,** 445 (1977); consequently, their estimate of processing capabilities of 10^{10} bits is grossly overstated.
5. M. J. Bage, and M. P. Beddoes, Appl. Opt. **15,** 2830 (1976).
6. D. J. Raso, J. Opt. Soc. Am. **58,** 432 (1968).
7. J. N. Latta, Appl. Opt. **10,** 2698 (1971); J. N. Latta and R. C. Fairchild, Soc. Photo-Opt. Instrum. Eng. **39,** 107 (1973).
8. K. von Bieren, Appl. Opt. **10,** 2739 (1971).
9. A. Vander Lugt, Appl. Opt. **5,** 1760 (1966).
10. M. Chang, Appl. Opt. **10,** 2550 (1971).

Meetings Calendar *continued from page 626*

1979

April

1–6 Polymers for Optical Fiber Systems, ACS symp., Honolulu *M. J. Bowden, Bell Labs., 600 Mountain Ave., Murray Hill, N.J. 07974*

2–5 SPIE Tech. Symp. East '79, Hyatt Regency Hotel, Washington, D.C. *C. W. Haney, U.S. Naval Air Dev. Ctr., Warminster, Pa. 18974*

2–6 6th Internat. Vacuum Metallurgy Conf. on Special Melting and Metallurgical Coatings, San Diego *R. W. Buckman, Jr., P.O. Box 18006, Pittsburgh, Pa. 15236*

9–13 Laser Radiometry and Beam Diagnostics course, Denver *Laser Inst. of Am., P.O. Box 9000, Waco, Tex. 76710*

16–18 Wear of Materials, internat. conf., Dearborn *K. C. Ludema, Mech. Eng. Dept., U. of Mich., Ann Arbor, Mich. 48109*

17 **OSA-SAS Detroit Section mtg.** *R. E. Michel, Lawrence Inst. of Technol., 21000 W. Ten Mile Rd., Southfield, Mich. 48075*

19–20 Practical Application of Lasers in Manufacturing course, Stamford, Conn. *Coherent, Inc., 3210 Porter Dr., P.O. Box 10321, Palo Alto, Calif. 94303*

23–25 Developments in Semiconductor Microlithography—IV, San Jose Hyatt House, San Jose, Calif. *SPIE, P.O. Box 10, Bellingham, Wash. 98225*

23–26 APS mtg., Washington, D.C. *W. W. Havens, Jr., 335 E. 45th St., New York, N.Y. 10017*

23–27 Remote Sensing of Environment, 13th internat. symp., Ann Arbor *Environmental Res. Inst. of Mich., P.O. Box 8618, Ann Arbor, Mich. 48107*

23–27 Laser Application in Materials Processing course, San Francisco *Laser Inst. of Am., P.O. Box 9000, Waco, Tex. 76710*

24–25 Advances in Optical Production Technology seminar, Nat. Phys. Lab., Teddington *Sira Inst. Ltd., South Hill, Chislehurst, Kent BR7 5EH, England*

25–27 Modeling and Simulation, 10th ann. Pittsburgh conf., Pittsburgh *W. G. Vogt, 348 Benedum Eng. Hall, U. of Pittsburgh, Pittsburgh, Pa. 15261*

28–3 May 81st Annual Meeting and Exposition of the American Ceramic Society, Cincinnati *F. P. Reid, ACS, 65 Ceramic Drive, Columbus, Ohio 43214*

May

7–11 Infrared: Sources, Components, and Systems course, Dallas *Laser Inst. of Am., P.O. Box 9000, Waco, Tex. 76710*

13–17 SPSE 32nd Ann. Conf., Boston Park Plaza Hotel, Boston *SPSE, 1411 K St. N.W., Suite 930, Washington, D.C. 20005*

15 **OSA-SAS Detroit Section mtg.** *R. E. Michel, Lawrence Inst. of Technol., 21000 W. Ten Mile Rd., Southfield, Mich. 48075*

15–16 **Gradient Index Optical Imaging Systems, OSA Topical Mtg.,** U. of Rochester *OSA, 2000 L St. N.W., Suite 620, Washington, D.C. 20036*

continued on page 659